Tectonophysics 923 (2026) 231069

Contents lists available at ScienceDirect

Tectonophysics

journal homepage: www.elsevier.com/locate/tecto

Seismic source parameters analysis in Southeastern Alps and associated tectonic implications

L. Moratto *, F. Abdi, A. Saraò

National Institute of Oceanography and Applied Geophysics - OGS, Italy

ARTICLE INFO

Keywords:
Seismic source parameters
Spectral inversion
Stress drop
Apparent stress
Seismic efficiency
Northeastern Italy seismicity

ABSTRACT

We present a comprehensive analysis of earthquake source parameters in the Southeastern Alps, a tectonically complex region located at the junction of the Eastern Alps and the Dinarides. Using single station spectral inversion of S-wave displacement spectra from 1521 well-recorded earthquakes ($1.3 \leq M_W \leq 4.3$) occurring between 2016 and 2023, we estimated seismic moment, corner frequency, static stress drop, apparent stress, radiated energy, and seismic efficiency. Our results reveal a small deviation from self-similar scaling condition, with static stress drop values ranging mostly from 0.1 to 10 MPa (median $\approx$ 0.84 MPa) and apparent stress stabilizing above 1 MPa for moderate events. The Savage-Wood efficiency values suggest a dominant overshoot rupture regime, indicating that only a fraction of the available stress is radiated as seismic energy. The spatial patterns of stress drop and attenuation correlate with the underlying tectonic domains. Regions characterized by strong, competent crust exhibit higher stress drops and lower attenuation, whereas areas with fractured, fluid-rich fault zones show lower stress drops and stronger attenuation. This study highlights the value of high-resolution spectral analysis and dense seismic networks for characterizing rupture processes and provides a new regional reference dataset for ground motion prediction and seismic hazard assessment in Southeastern Alps and comparable intraplate environments.

1. Introduction

The Southeastern Alps represent one of the most seismotectonically complex regions in Europe, shaped by the ongoing convergence of the Eurasian and Adriatic plates. This convergence has produced dense thrust, strike-slip, and extensional fault systems (Slejko et al., 1989; Bressan et al., 2003; Sara1ò et al., 2021). While seismicity in the region is typically moderate (rarely exceeding M_W 5.5), the area experiences a high rate of low-to-moderate magnitude earthquakes, offering a unique opportunity to investigate rupture processes across varied tectonic settings. The 1976 Friuli earthquake (M_S 6.5), which caused nearly 1000 casualties (Aoudia et al., 2000), remains a landmark event underscoring the significant seismic hazard of the region.

Understanding the rupture behavior of even smaller events across this structurally diverse region is essential not only for seismic hazard assessment but also for tectonic interpretation. In this context, the characterization of seismic source parameters such as seismic moment, corner frequency, stress drop, and radiated energy, is critical. These parameters provide fundamental insights into earthquake scaling laws, fault mechanics, and crustal properties, and are also crucial for developing ground motion prediction equations, modeling the spatio-temporal evolution of faulting, and assessing rupture efficiency. Such information enhances both theoretical understanding and applied seismic hazard models for this intraplate domain.

Previous investigations in the region have provided valuable, albeit fragmented, insights into source characteristics. Franceschina et al. (2006) analyzed 53 local events ($2.0 < M_L < 5.7$), estimating source spectra using the methods of Andrews (1986) and least-squares inversion. Bressan et al. (2007) focused on seismic swarms in Friuli and western Slovenia, contributing to the understanding of source variability in clustered sequences. More recently, Cataldi et al. (2023) applied parametric spectral inversion to 23 earthquakes ($2.3 \leq M_L \leq 4.5$) that occurred in Northeastern Italy between 2009 and 2019. Still, rapid magnitude and moment estimations based on response spectra have been explored at both regional scales (Moratto et al., 2017; Tarchini et al., 2025) and in microseismic settings (Moratto et al., 2019; Lanzoni et al., 2020). Despite these contributions, a comprehensive and spatially resolved analysis encompassing the broader Southeastern Alps

* Corresponding author.
E-mail address: lmoratto@ogs.it (L. Moratto).

https://doi.org/10.1016/j.tecto.2026.231069
Received 27 August 2025; Received in revised form 31 December 2025; Accepted 3 January 2026
Available online 6 January 2026

is still lacking.

This study aims to address that gap by conducting a region-wide spectral characterization of earthquake sources in the Southeastern Alps. Specifically, we aim to i) provide high-quality source parameters to be used in seismic hazard models tailored to the study zone, and ii) identify systematic variations in stress drop and rupture efficiency across distinct tectonic domains.

To achieve these goals, we apply parametric spectral inversion to a curated dataset of 1521 earthquakes ($1.3 \leq M_W \leq 4.3$) recorded in the region between 2016 and 2023. The resulting catalog includes estimates of seismic moment (M_0), corner frequency (f_C), source radius (a), radiated energy (E_R), static stress drop ($\Delta\sigma$), apparent stress (τ_a), and seismic efficiency (η_{SW}), and is available on Zenodo (Moratto et al., 2025a).

As noted in many studies (e.g. Abercrombie, 2021; Bindi et al., 2024), some source parameters, particularly stress drop, remain among the most uncertain in seismology. These estimates are highly sensitive to methodological choices, including attenuation correction, source model assumptions, and spectral fitting procedures. A recent validation study (Abercrombie et al., 2025 and reference therein), shows that applying different methods to the 2019 Ridgecrest sequence, can produce stress drop values differing by more than an order of magnitude, highlighting the need for regionally calibrated and consistent approaches. Importantly, Abercrombie et al. (2025) concluded that no single method consistently outperforms others; rather, reliable and robust stress drop estimates are achieved by selecting techniques that are best suited to the available data and the specific tectonic context, while explicitly considering their inherent trade-offs. According to their findings, the most trustworthy results are obtained not by relying on a single approach, but by integrating multiple methods to mitigate method-dependent biases and uncertainties. In this framework, the detailed dataset we present provides a valuable foundation for future efforts aimed at refining source parameter estimates and improving the overall characterization of seismicity in the study area.

For our study we used the SourceSpec software (Satriano, 2024) - an algorithm among those analyzed in the study by Abercrombie et al. (2025) - that has proven effective for analyzing small-to-moderate earthquakes recorded by dense regional networks in tectonically complex areas. Through frequency-domain spectral inversion, we simultaneously estimated source parameters and path attenuation (t^*). This approach is particularly suitable for the Southeastern Alps, where variable crustal structures, depth-dependent attenuation, and diverse stress regimes coexist. Because our aim is to resolve large-scale spatial patterns of source parameters, we adopt a homogeneous processing workflow and rely on multi-station averaging to minimize local site effects.

In the following we detail the methodology and the dataset used and discuss the obtained results comparing them with previous studies in the area. By combining a dense seismic network, a robust inversion methodology, and a large, high-quality earthquake dataset, we aim to provide a solid spectral foundation for future seismic hazard modeling in this structurally complex region.

2. Method

We estimate the source parameters by inverting the displacement spectra using the SourceSpec software (version 1.8 release; Satriano, 2024). SourceSpec, developed in Python, is a well-documented, user-friendly, and actively maintained tool that is widely adopted by the seismological community. It has been successfully applied to earthquake sequences in a variety of tectonic settings around the world (Lengliné et al., 2023; Wang et al., 2023; Panebianco et al., 2023; Moratto et al., 2025b). This method utilizes Brune's classical model and performs parametric spectral fitting, in which observed displacement spectra are matched to theoretical source models assuming circular ruptures (e.g., Abercrombie, 1995; Zollo et al., 2014). The algorithm inverts P- or S-wave displacement amplitude spectra recorded at individual stations. For S-waves, the spectral model for each station, in M_0 units, can be written as:

$$M_X(f) = G(r)\cdot\frac{4\pi\rho_h^{\frac{1}{2}}\rho_r^{\frac{1}{2}}c_h^{\frac{5}{2}}c_r^{\frac{1}{2}}}{2R_{\theta,\varphi}} \bullet S_X(f) = M_0 \bullet \frac{1}{1+\left(\frac{f}{f_C}\right)^2} \bullet e^{-\pi f t^*} \tag{2.1}$$

where f is the frequency, $G(r)$ the geometrical spreading term, r the hypocentral distance, $R_{\theta,\varphi}$ the radiation pattern coefficient, ρ_h and ρ_r the medium densities at the hypocentre and the receiver, c_h and c_r the corresponding S-wave velocities, $S_X(f)$ the far-field Fourier displacement spectrum, f_C the S-wave corner frequency, and t^* the attenuation parameter.

Before performing the inversion, the spectral model is transformed into M_W units so that the observed spectrum is represented as:

$$Y_X(f) = \frac{2}{3} \bullet \left(\log_{10}\left(M_X(f)\right) - 9.1\right) \tag{2.2}$$

The three motion components are combined into a single data vector using the root-sum-of-squares, which is then compared with the theoretical model:

$$\mathrm{Y(f)} = \frac{2}{3}\left[\log_{10}\left(\mathrm{M_0} \bullet \frac{1}{1+\left(\frac{\mathrm{f}}{\mathrm{f_C}}\right)^2} \bullet \mathrm{e}^{-\pi \mathrm{f} t^*}\right) - 9.1\right]$$

$$= \frac{2}{3}\left(log_{10}(M_0) - 9.1\right) + \frac{2}{3}\left[log_{10}\left(\frac{1}{1+\left(\frac{f}{f_C}\right)^2}\right) + log_{10}\left(e^{-\pi f t^*}\right)\right] \tag{2.3}$$

ultimately yielding the following model used in the inversion:

$$Y(f) = M_W + \frac{2}{3}\left[-log_{10}\left(1+\left(\frac{f}{f_C}\right)^2\right) - \pi f t^* log_{10}(e)\right] \tag{2.4}$$

with:

$$M_W = \frac{2}{3}\left(log_{10}(M_0) - 9.1\right) \tag{2.5}$$

The source parameters estimated simultaneously include M_0, f_C, source radius, static stress drop, and E_R. The attenuation parameter t^*, related to the seismic quality factor (Q_0), is also estimated and is allowed to vary for each source-receiver path to account for spatial variability along the ray paths. The resulting t* values are then converted to Q_0 using the following relation:

$$Q_0 = \frac{tt(r)}{t^*} \tag{2.6}$$

where tt is the travel time from source to station and r is the hypocentral distance. It is important to note that Q_0 is not treated as frequency dependent as shown in formula (2.6). We initialize the inversion using t^*, because SourceSpec performs the spectral fitting directly in terms of path-integrated attenuation (2.1), making t^* the natural parameter in the inversion space. The initial t^* value simply provides a numerical starting point for the inversion.

The source radius (a) is computed from f_C estimated from the spectral inversion:

$$a = k\frac{c_h}{f_C} \tag{2.7}$$

where c_h is the S-wave velocity at the hypocenter, and k is a constant which depends on the source model. The static stress drop ($\Delta\sigma$) is calculated from M_0 assuming a circular rupture of radius a (Madariaga, 2011):

$$\Delta\sigma = \frac{7}{16} \bullet \frac{M_0}{a^3} \tag{2.8}$$

The E_R is computed from the energy flux recorded at appropriate distances from the source, following the procedures described by Boatwright et al. (2002) and Lancieri et al. (2012), and including corrections for noise and bandwidth. The apparent stress (τ_a) is then defined as the product of the shear modulus and the ratio of E_R to M_0 (Wyss, 1979). Finally, the Savage-Wood seismic efficiency is calculated following Beeler et al. (2003), as the ratio of apparent stress to static stress drop.

A full grid search is performed to explore all possible parameter combinations (M_0, f_C, t^*) and identify the best-fitting solution for each individual spectrum. Each spectrum is inverted independently at single-station level allowing the moment magnitude (M_W) and f_C to be estimated separately for each record. Final event parameters are obtained by averaging only the stable solutions across stations, which reduces the influence of low SNR data and local path or site anomalies. Uncertainties are derived from the variability of the station-based estimates: the distribution of these values is used to compute the mean and standard deviation, in logarithmic space for f_C, which is approximately log-normally distributed.

This approach avoids mixing path-dependent attenuation effects that would arise if spectra or waveforms were averaged prior to inversion and helps limit the classical corner-frequency/attenuation trade-off (Scherbaum, 1990, 1994), as attenuation is treated separately for each path and the inversion is constrained within physically motivated bounds. The associated uncertainties reflect model simplifications and unmodeled effects in source (e.g. rupture velocity, radiation pattern), path (e.g. 3D heterogeneities), or site response. Key methodological challenges include the selection of appropriate time windows and accurate modeling of frequency-dependent attenuation and site effects. Because the aim of this study is to identify large-scale spatial patterns rather than optimize individual station estimates, the combination of single-station inversion and robust multi-station averaging ensures methodological consistency and reliability across the heterogeneous study area.

In this study, only S-waves were used because their larger amplitudes provide higher signal-to-noise ratios and more reliable parameter estimates. SourceSpec was configured following Panebianco et al. (2023). Initial values for M_W and f_C were automatically estimated by the software, while inversion bounds for M_W allowed variations of ±0.35 around the initial estimate and f_C was constrained between 1 and 45 Hz.

The starting value of t^* was manually assigned (0.03 s), based on the elastic and anelastic properties of the region. The bounds imposed on t^* (0.01–0.09 s) reflect the physically plausible range for the study area, considering hypocentral distances of 20–80 km, an average S-wave velocity of ~3.5 km/s, and regional $Q_0 \approx 260$ (Malagnini et al., 2002). These constraints prevent the inversion from exploring unrealistic combinations of very high corner frequencies and negligible attenuation (or vice versa), thereby reducing the classical f_C –t^* trade-off and stabilizing the inversion.

All waveforms were first processed using a bandpass filter with a lower cut-off of 0.8 Hz and an upper cut-off of 45 Hz, close to the Nyquist frequency for 100 Hz sampling. The inversion was performed only for stations with a minimum signal-to-noise spectral ratio (SNR) of 5. The signal-to-noise ratio was computed as the ratio between the RMS amplitude within the selected S-wave (or P-wave) window and the RMS amplitude within the pre-event noise window. The S/N > 5 threshold refers to the average spectral signal-to-noise ratio over the full inversion bandwidth (0.8–45 Hz). Only traces meeting this requirement across the entire frequency range were retained, preventing low- or high-frequency contamination from biasing the inversion.

Spectral amplitudes were computed using a 2.0 s time window for both S-wave and noise segments. The noise window begins 3.0 s before the P-wave arrival, ensuring a clean and uncontaminated portion of the record for estimating the background noise level. The pre-S interval was not used because it may contain P-wave coda and scattered phases, especially at short epicentral distances, which could artificially increase the estimated noise and bias the signal-to-noise ratio. The S-wave window starts 0.4 s before the S-wave arrival, preventing contamination from the preceding portion of the seismogram. The geometrical spreading coefficient is represented as r^n where n is fixed to 1, consistent with body-wave propagation in a homogeneous full space.

3. Data

The data used in this study are recorded from the OX seismic network, operated by the Seismological Research Centre (CRS) of the Istituto Nazionale di Oceanografia e di Geofisica Sperimentale (OGS). The OX network consists of 42 permanent seismological stations (Bragato et al., 2021), covering an area that extends from Lake Garda to the Italian - Slovenian border, and from the Po River to the Italian - Austrian border (Fig. 1). To enhance both spatial coverage and detection capabilities, the OX network is integrated in real time with more than 100 seismic stations from adjacent regional and national networks (see Data Availability). This integration has significantly improved detection sensitivity, allowing the system to record even negative-magnitude events when the interstation distance is below 10 km (Moratto and Sandron, 2015).

Over the last eight years, the network has enabled the manual review and archiving of more than 11,000 seismic events, providing a rich dataset for high-resolution spectral analysis in this tectonically complex region. For this study, we selected a subset of earthquakes that occurred between 1 January 2016 and 31 December 2023, within the spatial bounds of 44.5°- 47.0°N latitude and 10.0°-14.5°E longitude (Fig. 1). The locations and magnitudes of the events were obtained from the OGS bulletins (Snidarcig et al., 2017, 2018, 2019, 2020, 2021, 2022; Brondi et al., 2024, 2025). The corresponding velocimetric waveforms were retrieved and processed according to the procedures described in Tarchini et al. (2025). These include instrumental correction, bandpass filtering, and proper formatting of station and event headers. The final set of corrected waveforms, along with associated metadata, is available in a public repository (Moratto et al., 2024) and serves as the basis for the spectral inversion and source parameter analysis presented in this study.

The increasing complexity and variability of stress drop scaling at low magnitudes is well known and emphasises the importance of

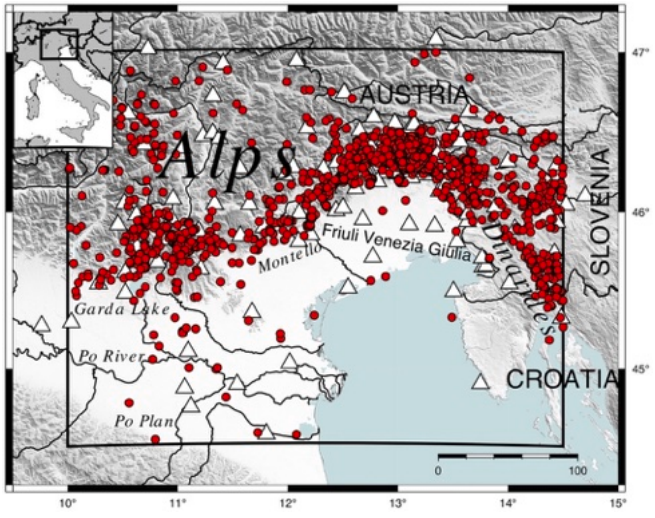

Fig. 1. Map of the seismicity analyzed in this study; the earthquakes (represented by circles) are taken from the OGS bulletins. The triangles show the utilized stations, while the black rectangle marks the study area monitored by the OGS.

defining reliability thresholds in spectral analyses (e.g., Bindi et al., 2020), especially due to enhanced attenuation effects and to mitigate saturation effects often observed in microseismic events (e.g., Abercrombie et al., 2017; Deichmann, 2018). To reduce contamination of the P- and S-wave windows by secondary arrivals, we restricted our dataset to events with hypocentral distances less than 80 km (Bragato et al., 2011). Furthermore, we restricted the analysis to those earthquakes for which Tarchini et al. (2025) estimated M_W (derived from SA) ≥ 1.5. This threshold also reflects the limitations imposed by the 100 Hz sampling rate of the OX network, which limits the resolution of the high-frequency spectral content and reduces the reliability of the source parameter estimates for smaller events. After applying these selection criteria, the resulting dataset comprises 4326 earthquakes within the study region. After applying SourceSpec the inversion successfully converged for 3406 events (~79 %), while 920 events did not yield valid solutions. Finally, we retained only events inverted at a minimum of five stations and with estimated $f_C \leq 35$ Hz. This additional selection further narrowed the dataset, resulting in a final set of 1521 earthquakes (Fig. 1), obtained by inverting a total of 13,882 waveforms; the final dataset spans a magnitude range of $1.3 \leq M_W \leq 4.3$.

4. Results and discussion

Using the selected 1521 events we derived key source parameters through spectral inversion, and the complete set of results is made available in an open dataset (Moratto et al., 2025a). To evaluate the robustness of the estimated parameters, we performed consistency checks by comparing our results with those reported in previous studies, where available. These comparisons provide valuable insight into the reliability of our methodology and help assess potential biases. In the following sections, we detail the distribution of the estimated parameters and discuss their physical implications in the context of regional seismotectonics.

Fig. 2 shows an example of the displacement amplitude spectra calculated with the SourceSpec code for the source parameters inversions related to an earthquake occurred on 11 March 2023.

4.1. Moment magnitude

To validate the M_W estimates obtained in this study (M_W(SS)), we compared them with those derived from spectral acceleration (M_W(SA); Moratto et al., 2017; Tarchini et al., 2025) and from moment tensor solutions (M_W(MT)) for events with $M_W \geq 3.5$ (Saraò et al., 2021).

We observe a generally good agreement between M_W(SS) and the independent values derived from the moment tensor solutions (M_W(MT); Fig. 3a) and from the spectral acceleration (M_W(SA); Fig. 3b). Most residuals fall within ±0.3, consistent with the expected uncertainty of both reference methods.

Although site effects were not explicitly corrected in this study – a full + characterization of site response across all networks, while valuable, is beyond the scope of this work and would require a dedicated analysis - several considerations support the robustness of our magnitude estimates. Most stations of the OX network, as well as the majority of those from the additional networks used here, are installed on rock or stiff soil (Priolo et al., 2015; Klin et al., 2021), where local amplification is expected to be limited. The intra-event variability of the single-station inversions is generally limited. For the entire dataset, M_W values from different stations cluster around a stable central value, with a typical standard deviation of $s[M_W] \approx 0.19$. A similar behavior is observed for the estimated corner frequencies, with $s[log10(f_C)] \approx 0.24$. These variability levels are comparable to previous spectral studies of microearthquakes in northeastern Italy and suggest that path-dependent

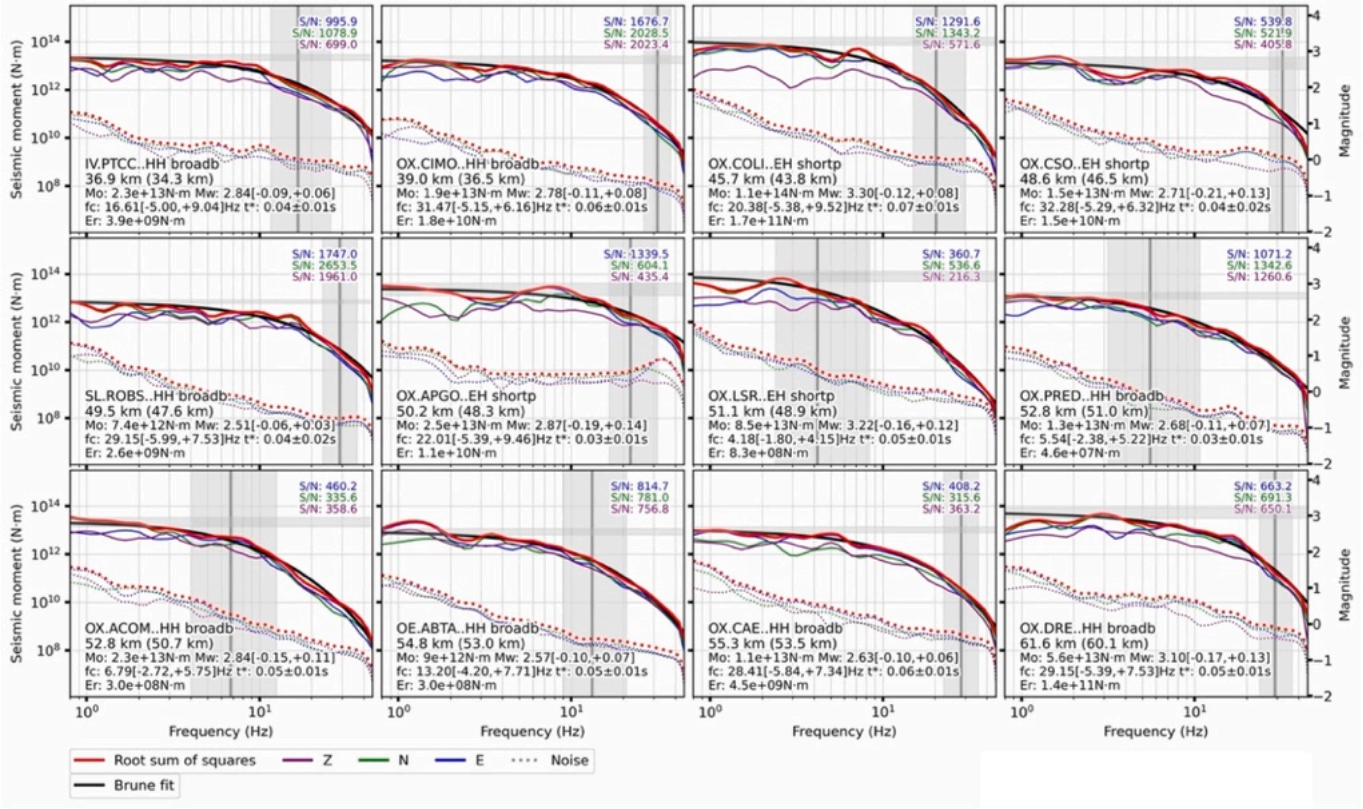

Fig. 2. Displacement amplitude spectra were computed using the SourceSpec code for the inversion of source parameters. The figure displays both signal spectra (solid lines) and noise spectra (dashed lines), together with the inverted source parameters for each seismic station. The corrected signal root-sum-of-squares spectrum (red solid line) was selected as the input for the inversion. The spectral fitting was performed against the Brune source model (black solid line), shown for comparison. (For interpretation of the references to colour in this figure legend, the reader is referred to the web version of this article.)

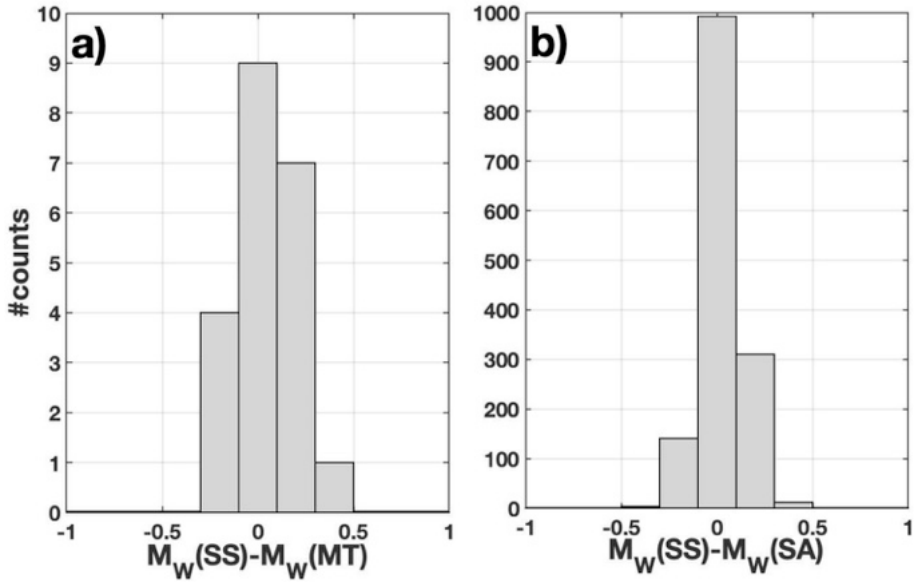

Fig. 3. Distribution of the residuals for the comparison between: a) M_W(SS) and M_W(MT) for the seismic events with $3.5 \leq M_W \leq 4.0$; b) M_W(SS) and M_W(SA) for all considered dataset.

attenuation or site effects do not dominate the event-level estimates.

A notable exception is a single event located in the Po Plain, which displays a residual of +0.4 in both comparisons. In this case, M_W(SS) overestimates the magnitude (4.3) relative to M_W(MT) and M_W(SA) (both 3.9), likely due to unmodelled site amplification. Indeed, while many stations are on rock or stiff soil, some are installed within the Po Plain, where significant site effects may enhance ground motion and bias the moment, and therefore M_W(SS), upwards, as illustrated by this outlier.

Fig. 4 shows a direct comparison between M_W(SS) and M_W(SA). The distribution of the data indicates a strong agreement between the two estimates from about $M_W = 1.3$ to $M_W = 4.0$. The scatter is limited and symmetrical, with most data points lying within ±0.3 magnitude units, which is consistent with the uncertainty associated with the M_W(SA) estimates. A small number of outliers appear in the higher magnitude range, including a point around M_W(SS) ≈ 4.3 which corresponds to the anomalous event in the Po plain that we have already discussed.

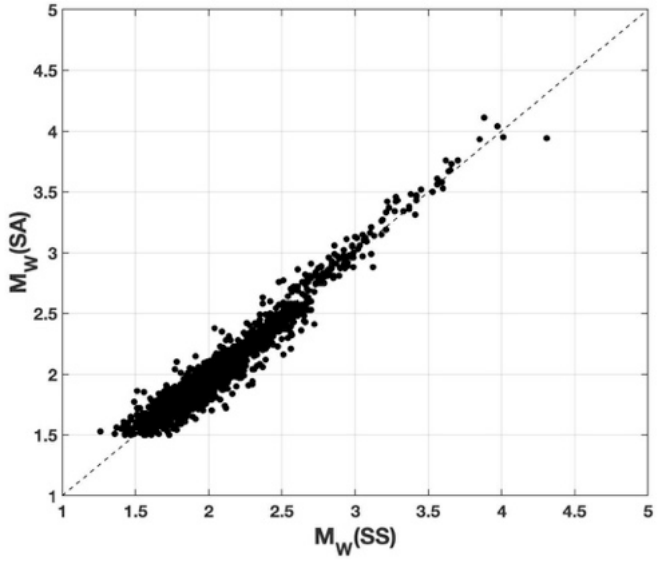

Fig. 4. Comparison between M_W(SS) and M_W(SA) for 1521 earthquakes in northeastern Italy. The dashed line indicates the 1:1 correspondence.

4.2. Attenuation

An intrinsic trade-off exists between source and path effects, which can influence the estimation of source parameters (e.g. Bindi et al., 2020). In particular, f_C and t^*, both affecting the high-frequency content of the signal, may compensate for each other during the inversion process. In contrast, M_W and M_0 are more stable and less sensitive to this trade-off. Despite the potential coupling between f_C and t^* values, our dataset does not show any evident correlation between the two parameters, suggesting they are estimated independently. This is illustrated in Fig. 5a, where no specific trend can be recognized. The apparent alignment of some data points originates from the discrete sampling of both parameters in the grid-search inversion, which can produce clusters of identical or neighbouring values. To further evaluate how well the attenuation term is resolved along comparable ray paths, we performed an additional test analogous to the approach of Jozi Najafabadi et al., (2023). The study region was divided into 5 × 5 × 3 km spatial cells, and for each cell we selected t^* estimates from at least two earthquakes recorded at the same station, yielding 8804 measurements grouped into 1450 cells. The intra-cell distributions show that t^* is highly stable for closely spaced events travelling along similar paths, with typical standard deviations of ~0.006 s. As shown in Fig. 5b and c neighbouring events recorded at the same station exhibit nearly identical attenuation along common ray paths, confirming that t^* is consistently resolved and not dominated by station- or path-specific anomalies.

Building on this, we now examine the spatial distribution of attenuation, expressed as a path-averaged Q_0 value derived from the t^* estimates for each source–receiver pair (Fig. 6a). In our dataset, Q_0 has a median of 309 (interquartile range: 207–466), consistent with previous studies in the region (Malagnini et al., 2002). Fig. 6a shows the spatial distribution of Q_0, derived from the t^* for each source–receiver pair, in the investigated area. Lateral variability in attenuation appears from western to eastern margins, with higher Q_0 values ($Q_0 > 550$) observed around the Montello area suggesting more efficient wave propagation in those domains; lower Q_0 values ($Q_0 < 400$) predominantly characterizes the central sector of the study area, particularly along the Alpine arc, reflecting more attenuative crustal structures, possibly due to higher sediment thicknesses, fluid content, or structural heterogeneity. This pattern is consistent with previous studies suggesting that Q_0 in the Eastern Southern Alps is strongly controlled by lithological contrasts,

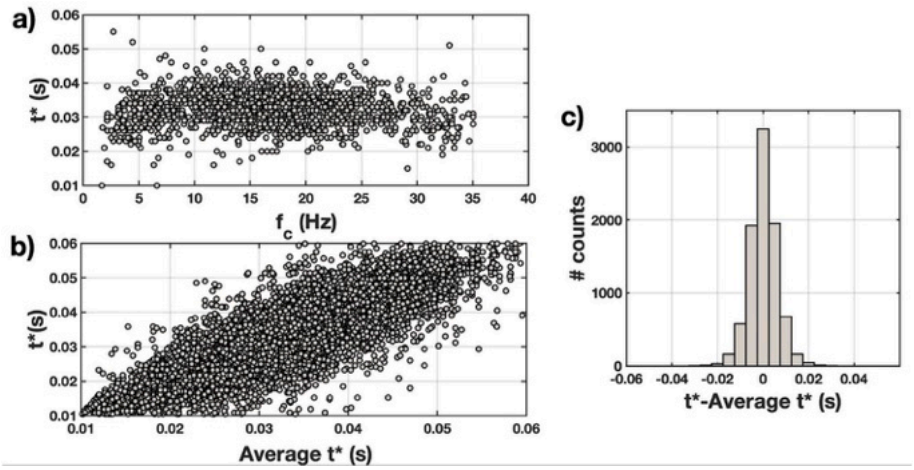

Fig. 5. a) Distribution of f_C vs event-averaged t^* for the entire dataset. b) t^* values plotted against the average values along common ray paths computed within 5x5x3 km spatial cells; c) histogram of residuals defined as t^*-average(t^*) for all common ray paths.

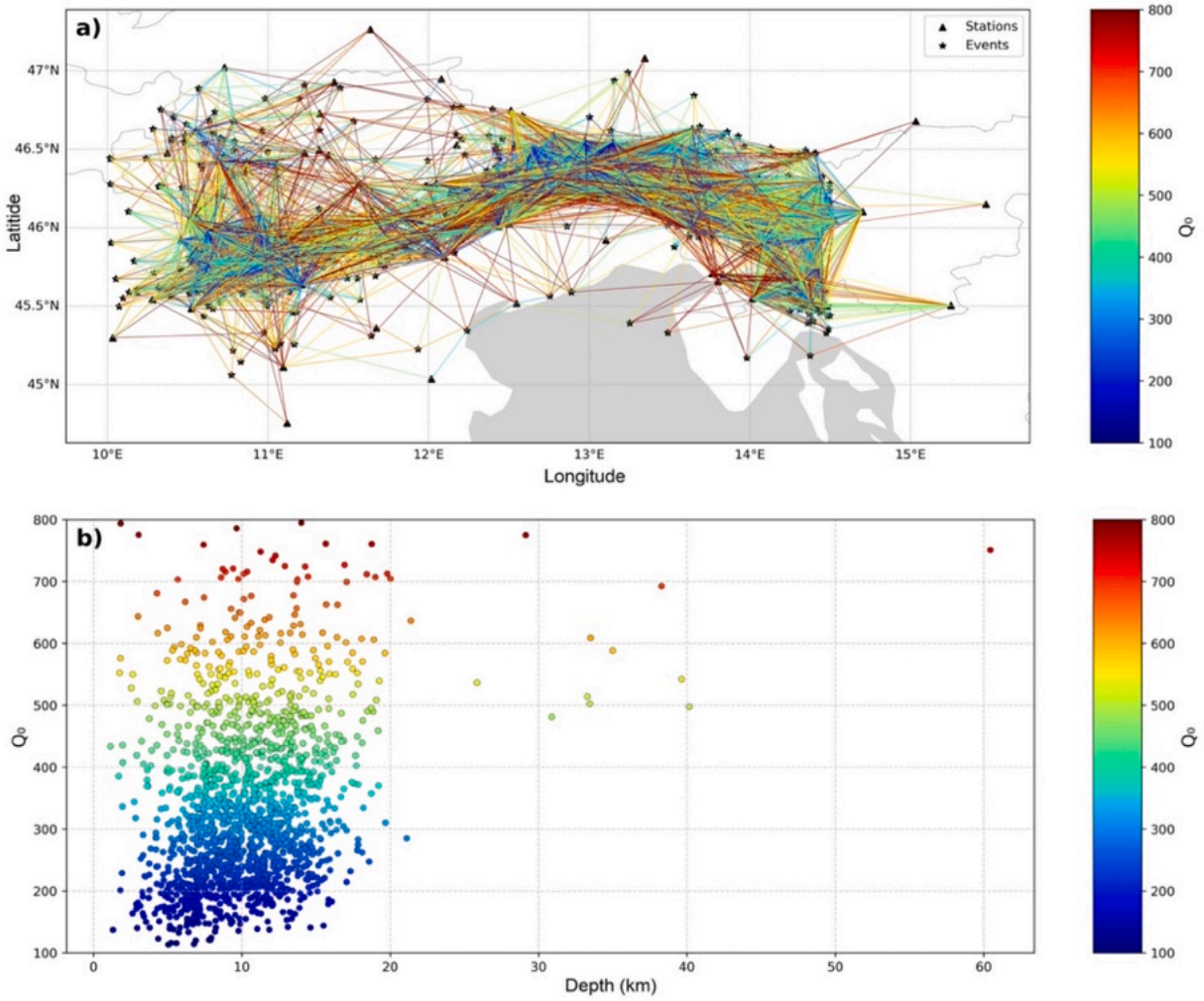

Fig. 6. a) Spatial distribution of Q_0 values estimated in this study. Each line represents the Q_0 value computed along each source-to-receiver path, colour-coded according to the corresponding attenuation strength. Higher Q_0 values (red hues) indicate lower attenuation, whereas lower Q_0 values (blue hues) correspond to stronger attenuation. b) Q_0 values plotted as a function of earthquake hypocentral depth for the analyzed dataset. (For interpretation of the references to colour in this figure legend, the reader is referred to the web version of this article.)

crustal composition, and tectonic regime. A similar trend emerges from the Q_P 3D-model proposed by Jozi Najafabadi et al. (2023), where lower Q_P values are located in central Friuli and higher Q_P characterizes the Montello zone. The deeper earthquakes (depth > 20 km), primarily

located in the Po Plain, tend to exhibit Q_0 values exceeding 500 (Fig. 6b), further supporting the link between depth, structural setting, and attenuation characteristics. In particular, most events are concentrated between 5 and 20 km depth, where Q_0 ranges predominantly from 100 to 800. The overall trend highlights substantial variability but does not indicate a strong systematic dependence on depth, supporting the interpretation that lateral heterogeneity plays a larger role than vertical gradients in the attenuation structure of the region.

The observed spatial heterogeneity supports the use of path-dependent attenuation corrections in spectral inversion and underscores the importance of regional calibration in source parameter estimation, in line with recent findings by Bindi et al. (2024) and Yen et al. (2024). In particular, Yen et al. (2024) emphasize that using region-specific attenuation models is essential to avoid biases in stress drop estimates, especially in tectonically complex areas such as the Southeastern Alps. Joint inversion strategies that incorporate a more explicit representation of the attenuation structure (e.g. Rietbrock, 2001; Eberhart-Phillips and Chadwick, 2002) represents a promising direction for future developments, as it would allow a refined characterization of attenuation structure and potentially reduce residual path-related variability in the source parameters.

4.3. Stress drop

The seismic source parameters derived from the spectral analysis reveal a wide range of event sizes and corner frequencies. As shown in Fig. 7a, M_0 ranges from 1×10^{11} to 3.7×10^{15} Nm, corresponding to M_W between 1.3 and 4.3. The associated f_C span from 1.7 to 35 Hz. From these, source radii were inferred, ranging from 33 to 780 m, with a median of 74 m and 68 % confidence limits between 43 and 126 m (Fig. 7b).

The attenuation-related decay of high-frequency amplitudes appears less pronounced and the saturation effect is not clearly visible in Fig. 7a. Weaker attenuation permits more reliable estimation of f_C and source parameters, even for low-magnitude events.

Indeed, following Kanamori and Rivera (2004), we performed a least-squares regression between $\log_{10}(M_0)$ and $\log_{10}(f_C)$, obtaining:

$$\log_{10}(f_c) = -0.2840(\pm 0.0002)^{*}\log_{10}(M_0) + 4.618(\pm 0.026) \quad (4.1)$$

The slope of −0.284 is slightly higher than the theoretical value of −1/3, which is expected under self-similarity conditions, where M_0 scales with f_C^{-3}. In our case, M_0 scales approximately with $f_C^{3.52}$, indicating a slight positive deviation from self-similarity, (quantified by a correction factor of 0.52). However, the lack of a clear magnitude dependence in $\Delta\sigma$, combined with the broad spread of stress drop values across the dataset, supports the interpretation that earthquake ruptures in the Southeastern Alps are approaching quasi self-similar behavior, with minor regional or scale-dependent variations. Such deviations have been previously reported in the area (Franceschina et al., 2006; Franceschina et al., 2013), and may be linked to factors such as fault zone maturity, rupture directivity, or spatial heterogeneity in stress and strength.

Static stress drops estimated using the Brune model range from 0.0014 to 42.08 MPa, with most values falling between 0.1 and 10 MPa. The median is approximately 0.84 MPa (interquartile range: 0.24–2.98 MPa). These values are broadly consistent with previous observations from northeastern Italy and other intraplate areas. Franceschina et al. (2006) reported values from 0.07 to 5.31 MPa (average 0.73 MPa), while Franceschina et al. (2013) estimated 4.9 MPa for the Kobarid mainshock and 0.03–1.55 MPa for its aftershocks. Similarly, Cataldi et al. (2023) found $\Delta\sigma$ predominantly between 1.5 and 6 MPa, with some exceeding 15 MPa in the Friuli Venezia Giulia region. In the Montello area, Moratto et al. (2019) reported lower $\Delta\sigma$, with a median of 0.45 MPa based on the Madariaga model, a values that align with the lower bound of our distribution. Overall, smaller earthquakes in our dataset exhibit slightly lower $\Delta\sigma$ than larger events. For example, the strongest event ($M_W = 4.3$) shows a $\Delta\sigma$ of 3.95 MPa.

On a broader European scale, Yen et al. (2024) observed increasing $\Delta\sigma$ with magnitude, which stabilize beyond $M_W = 4$, indicating self-similar rupture behavior. Their median $\Delta\sigma$ of 13.8 MPa for larger events is comparable to the upper values observed in the Southeastern Alps. A similar variability has been documented in other intraplate regions. For instance, Saadalla et al. (2025) reported $\Delta\sigma$ from 0.04 to 16.3 MPa for earthquakes in the Dahshour region (M_L 1.7–3.6), underscoring that such variability is not confined to plate boundaries. Instead, it reflects the strong influence of local structural and rheological conditions on rupture dynamics.

The spatial distribution of $\Delta\sigma$ across the SE Alps region (Fig. 8a) reveals pronounced variability, spanning over three orders of magnitude, from $\Delta\sigma$~0.01 MPa to $\Delta\sigma$ >10 MPa. To interpret these patterns, the region was subdivided into three seismotectonic macro-areas (V, F, S) based on published zonations for northeastern Italy and western Slovenia. The V area follows the Veneto districts of Sugan and Peruzza (2011), while the F area corresponds to the central Friuli districts of

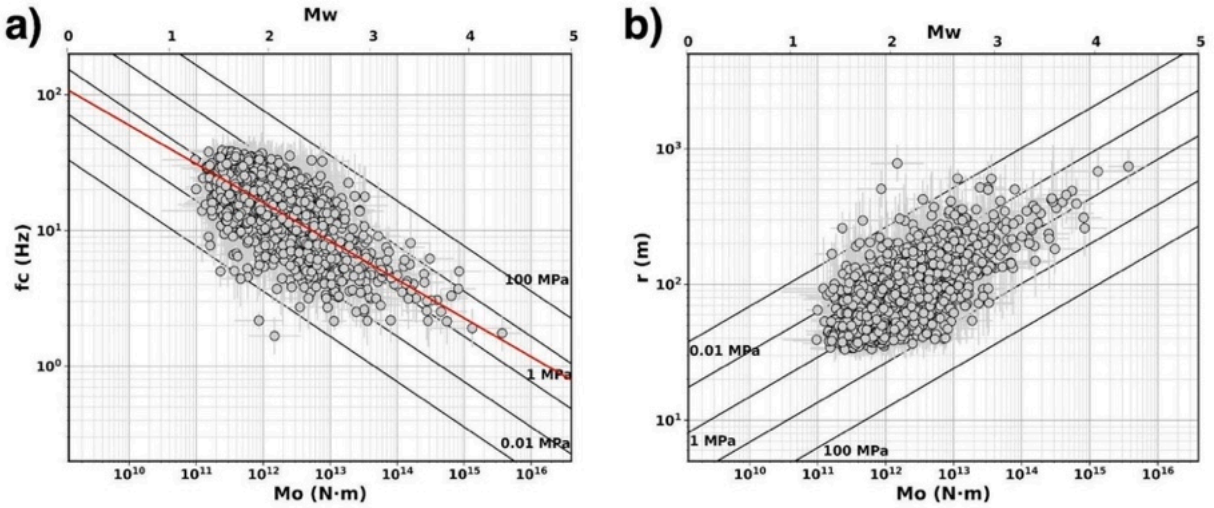

Fig. 7. a) Estimated M_0 and f_C for S wave together with the uncertainties obtained from analyzed data set; the solid lines refer to constant $\Delta\sigma$ expressed in MPa. Red line shows the fit line. b) Estimated M_0 and source radius together with the uncertainties obtained from analyzed data set; the solid lines refer to constant $\Delta\sigma$ expressed in MPa. (For interpretation of the references to colour in this figure legend, the reader is referred to the web version of this article.)

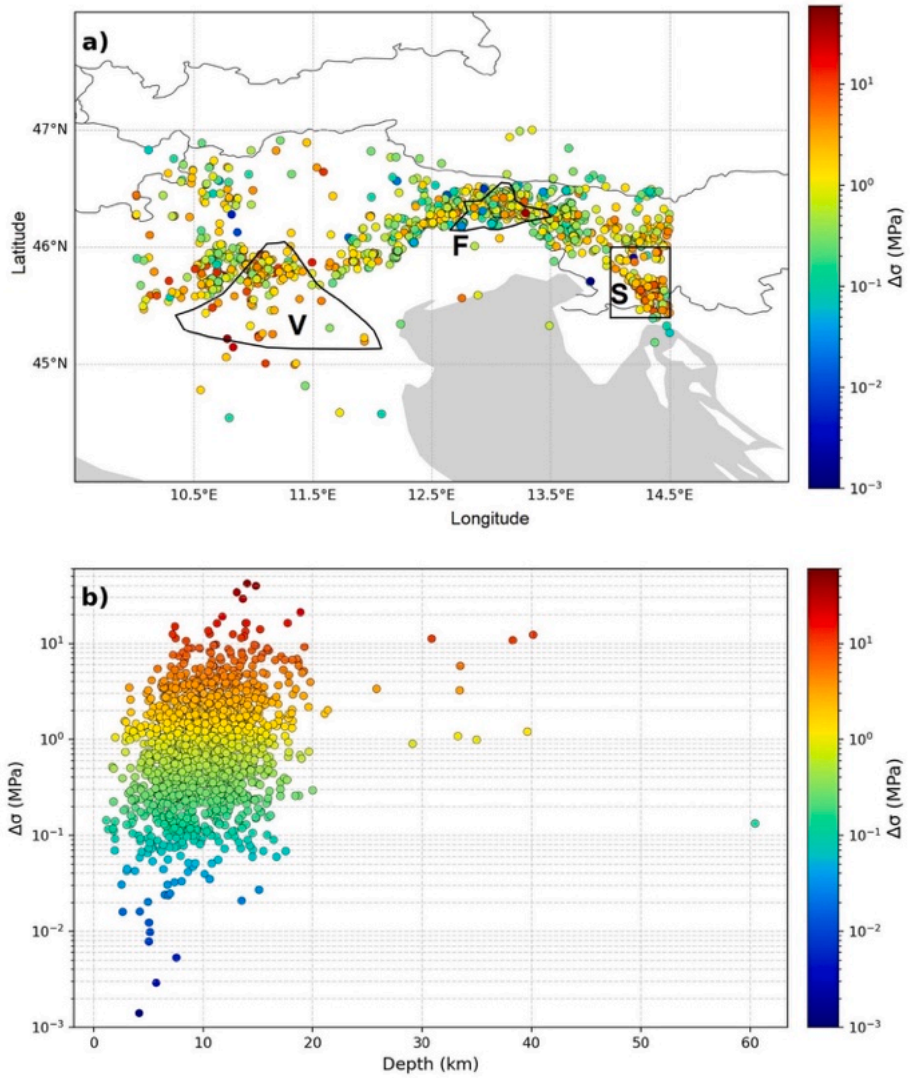

Fig. 8. a) Spatial distribution of static stress drop in the study area. The polygons refer to the Western Prealpine Sector (V); the Central Alpine Foreland (F); the Eastern Dinaric Margin (S). b) Static stress drop as a function of hypocentral depth.

Bressan et al. (2018, 2019); within this region, several adjacent districts defined by Bressan et al. (TOL, MN, GE, see their paper for details) were merged because they share homogeneous thrust-dominated deformation, similar focal-mechanism characteristics, and consistent spatial trends in upper-crustal elastic properties, and they lie within the sector of maximum expected peak ground acceleration in the Friuli Venezia Giulia seismic hazard map (Slejko et al., 2011). The S area, extending into western Slovenia, reflects the strike-slip seismotectonic domains described by Bressan et al. (2018) and captures the transition from the Alpine–Friulian compressional belt to the Dinaric strike-slip regime. These polygons therefore delineate geologically and seismologically coherent units for comparing source parameters.

Elevated values ($\Delta\sigma$ >1 MPa, shown in red tones) are concentrated in the eastern Southern Alps and Dinaric sectors, particularly at the Eastern Dinaric Margin (S zone), and in the Western Prealpine Sector (V zone). These areas may reflect enhanced strain energy release and stronger fault asperities. In contrast, lower stress drop values ($\Delta\sigma$ <0.1 MPa, in blue-green) are more prevalent in Central Alpine Foreland (F zone), potentially linked to low rupture velocity, high pore fluid pressure, or diffuse deformation along complex fault networks. Such spatial variations likely reflect differences in tectonic loading, lithospheric structure, and fault zone maturity. The presence of regionally distinct patterns reinforces the need for calibrated stress drop models in both seismic hazard assessment and ground motion prediction efforts. In terms of depth distribution (Fig. 8b), most events are located between 5 and 20 km, where $\Delta\sigma$ generally range from 0.1 to 10 MPa. Within this interval, no systematic depth-dependence is evident. However, two notable trends emerge: deeper events (>20 km) more frequently show $\Delta\sigma$ exceeding 1 MPa; very low stress drop events ($\Delta\sigma$ <0.02 MPa) occur exclusively at shallow depths (<10 km). This apparent increase in stress drop with depth is physically plausible, as higher confining pressure at depth may enhance normal stress on faults, allowing for more significant stress release (Abercrombie et al., 2021). However, this trend might also reflect methodological limitations, such as uncorrected depth-dependent attenuation or assumptions of constant rupture velocity across depth (Abercrombie, 2021). A smaller number of earthquakes at depths greater than 30 km show a wide range of $\Delta\sigma$ values, but due to the limited amount of data at this depth range, no clear conclusions can be drawn. Similar to our findings, Bindi et al. (2024) report that while localized depth-dependent variations in $\Delta\sigma$ may occur, the overall variability across Central and Southern Italy is dominated by lateral heterogeneity rather than systematic depth trends.

Looking at the regional detail (Fig. 9a–c), in the V zone (Fig. 9a), the median $\Delta\sigma$ is 1.9 MPa from 150 earthquakes ($1.6 < M_W < 3.9$). While for some events $\Delta\sigma < 1$ MPa, the majority indicate elevated stress release. This region includes part of the Po Plain, where deeper events are

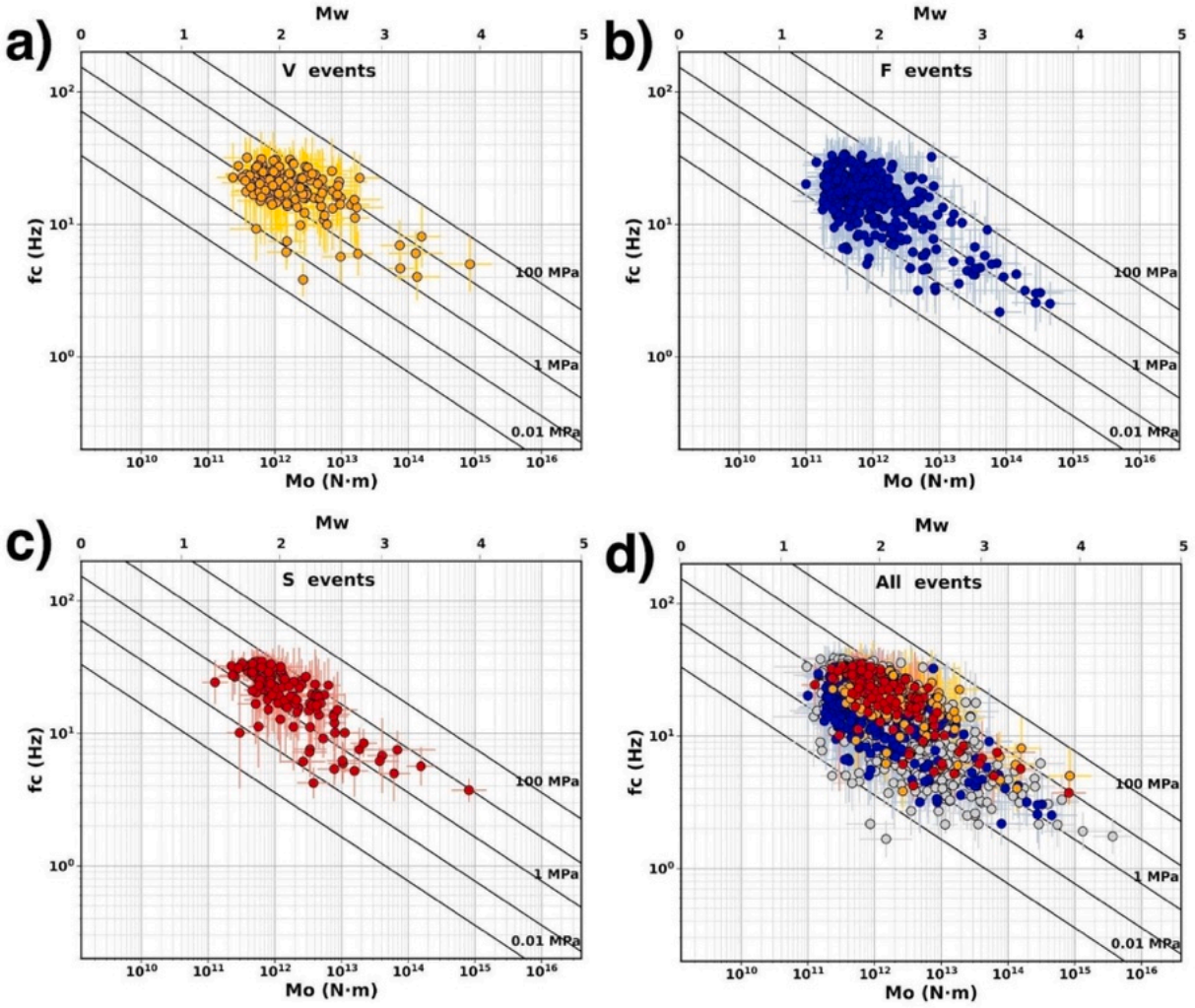

Fig. 9. f_C versus M_0 for the events analyzed in this study, shown on log-log axes. The top axis reports the equivalent M_W. Diagonal black lines indicate constant static stress drop levels of 0.01 MPa, 1 MPa, and 100 MPa, based on Brune's circular source model. a) Events located in the V (yellow), b) F (blue), c) and S (red) zones; d) All events combined, colour-coded by region: V (yellow), F (blue), S (red), and unclassified (gray).

common, likely contributing to the observed pattern. In the F region, $\Delta\sigma$ values are lower (Fig. 9b), with a median of 0.65 MPa based on 333 events with magnitudes from 1.5 to 3.7, roughly an order of magnitude lower than V and S. The S zone (Fig. 9c) exhibits a median $\Delta\sigma$ of 2.17 MPa, calculated from 129 events ($1.5 < M_W < 4.0$), with most earthquakes showing values. Fig. 9d shows the combined dataset from all three regions, illustrating a robust inverse relationship between M_0 and f_C, as expected from ω^2 source theory, which correlates well with regional tectonic and structural factors. High $\Delta\sigma$ zones are often linked to intact, competent rocks, lower fluid pressure, and longer interseismic intervals. This interpretation is consistent with earlier findings (Folesky, 2024; Moyer et al., 2018; Goebel et al., 2015). Fault properties including roughness, friction, and fluid saturation, also play a key role in stress accumulation and release (Jolivet and Frank, 2020).

Several studies (Pérez-Campos and Beroza, 2001; Zúñiga and Rodríguez-Pérez, 2025) emphasize the dependence of static stress drop on tectonic setting. Our study area, located at the junction of two major tectonic domains, the E–W-trending Alps and the NW–SE Dinarides (Slejko et al., 1989), exhibits distinct faulting regimes that appear to influence the observed stress drop distribution (Fig. 10a).

The ternary plots (Fig. 10b) illustrate the spatial variability in rupture styles across the study area. In the V zone, both strike-slip and reverse mechanisms are prevalent; F is dominated by thrust events with low-angle components; and S shows a predominance of strike-slip and normal faulting. This distribution closely correlates with the observed stress drop patterns (Fig. 9a). Specifically, the F zone, characterized primarily by reverse faulting, exhibits the lowest median stress drop, consistent with the global trend reported by Zúñiga and Rodríguez-Pérez (2025), who found that reverse events typically have lower static stress drops and release less seismic energy due to partial stress drop behavior. In contrast, the S region shows elevated stress drop values, reflecting its dominance of strike-slip faulting, which is commonly associated with higher rupture efficiency and overshoot mechanisms. The presence of some normal faulting events in this zone may further contribute to the high stress drop values, as Zúñiga and Rodríguez-Pérez (2025) reported that normal events tend to have higher dynamic stress drops than reverse ones. The V zone, which includes both reverse and strike-slip events, also exhibits relatively high stress drop values, likely driven by the contribution of strike-slip faulting.

Overall, our findings are consistent with the global synthesis by Zúñiga and Rodríguez-Pérez (2025), which demonstrated a systematic variation in stress drop with faulting mechanisms. This mechanism-dependent variability highlights the critical role of tectonic setting in shaping stress release characteristics and reinforces the importance of considering rupture style in stress drop estimation and seismic hazard assessments.

Fluids have a critical impact on rupture mechanics. Elevated pore fluid pressures reduce effective normal stress, promoting aseismic slip

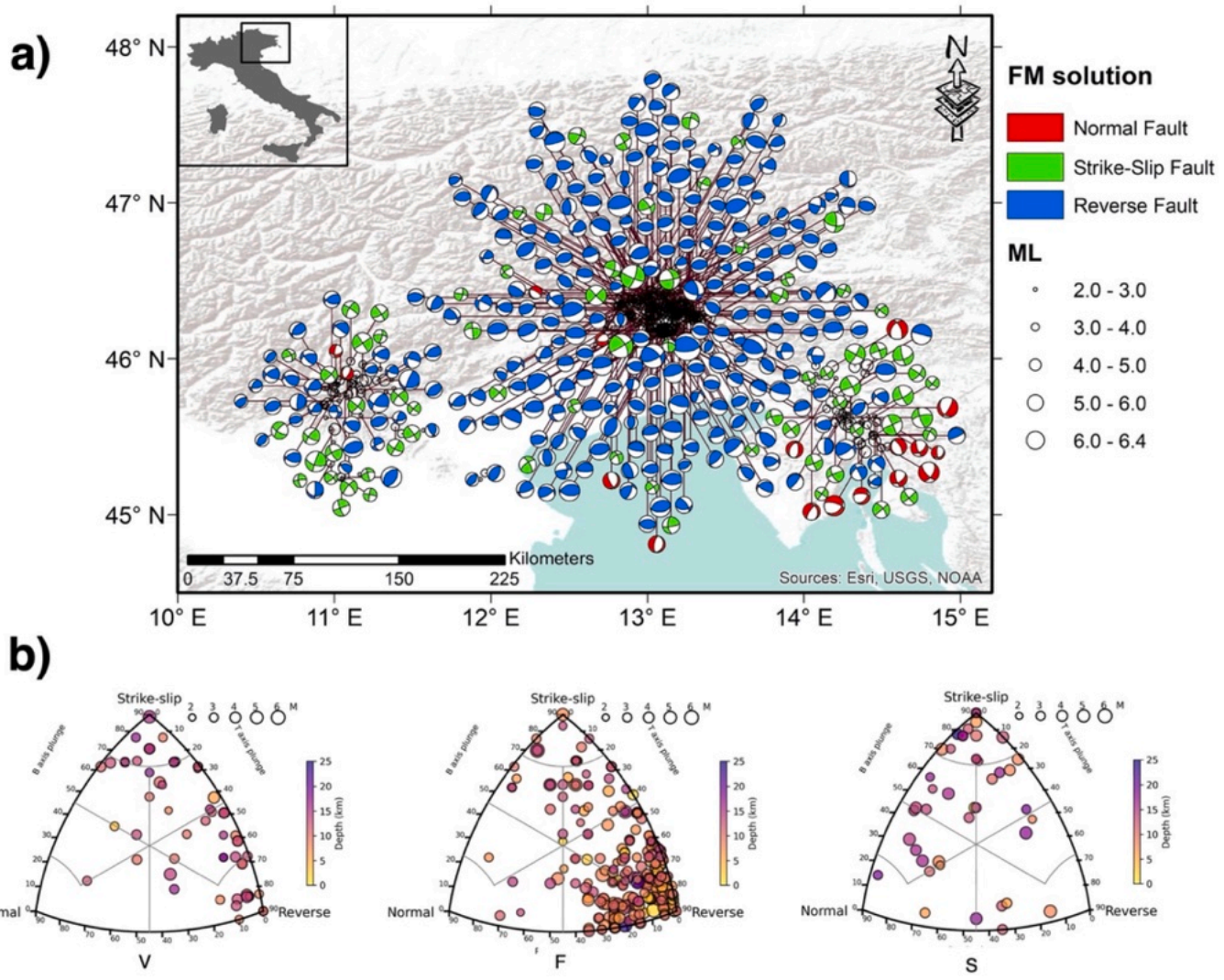

Fig. 10. a) Map and focal mechanism classification of earthquakes in the Southeastern Alps, based on the catalogs from Saraò et al. (2021) and Sugan et al. (2024) for the three main zones: V (western cluster), F (central cluster), and S (eastern cluster). b) Ternary diagrams showing the classification of faulting mechanisms for each zone based on the plunge of the P, B, and T axes. The colour scale represents the earthquake depth, while symbol size is scaled by magnitude.

and lowering stress drop values. This is evident in the F zone, which shows both low stress drop and low Q_0 values, markers of high seismic attenuation. Jozi Najafabadi et al. (2023) identified a strong anomaly in this region, with high attenuation, low V_P, and elevated V_P/V_S ratios, pointing to fluid-filled fractures and fault zones. These features enhance energy absorption and may promote earthquake swarms (Shearer et al., 2006; Oth, 2013). By contrast, the V and S zones exhibit higher stress drop values and lower attenuation. In V, this is supported by high Q values, while in S, high P-wave velocities and high Q (Rajh et al., 2024) suggest low fracture density and more efficient stress loading. Further supporting this interpretation, Goebel et al. (2015) noted that high stress drop earthquakes tend to occur in regions with greater shear resistance and longer recurrence intervals. In contrast, low stress drop events often arise in fault segments with high fluid content, damage zones, or elevated creep, which promote incomplete or inefficient rupture (Moyer et al., 2018).

Finally, static stress drop plays a critical role in shaping earthquake ground motion, and therefore has direct implications for seismic hazard analysis. Higher stress drop events are known to generate stronger ground velocities (Abercrombie, 2021), highlighting the importance of spatially resolving this parameter in hazard models.

4.4. Radiated energy

The E_R in our dataset spans from 1×10^4 to 1.2×10^{11} Nm (Fig. 11), covering nearly seven orders of magnitude. Apparent stress (τ_a) generally exceeds 1 MPa for events with $M_0 > 1 \times 10^{14}$ Nm and tends to decrease with decreasing moment. For smaller events, τ_a values as low as 0.01 MPa are observed. This trend may suggest lower radiation efficiency in smaller earthquakes, potentially due to increased energy dissipation at the source through processes such as cracking, inelastic deformation, or unmodeled path attenuation. These differences could reflect variations in rupture dynamics or complexity between small and large events and merit further investigation.

Our τ_a values are broadly consistent with previous findings. Franceschina et al. (2006) reported apparent stress values mostly between 0.1 and 1.0 MPa, while Franceschina et al. (2013) found values of 1.9 MPa for a mainshock and between 0.01 and 0.48 MPa for associated aftershocks. Similarly, Moratto et al. (2019) observed τ_a ranging from 0.01 to 1 MPa in the Montello area, with two larger events exceeding 1 MPa. The relationship between E_R and M_0 reflects a dynamic scaling behavior, as E_R represents the fraction of energy emitted as seismic waves during rupture. The ratio E_R/M_0 (commonly expressed via the scaling parameter $\tilde{e}$) offers insight into rupture efficiency and energy

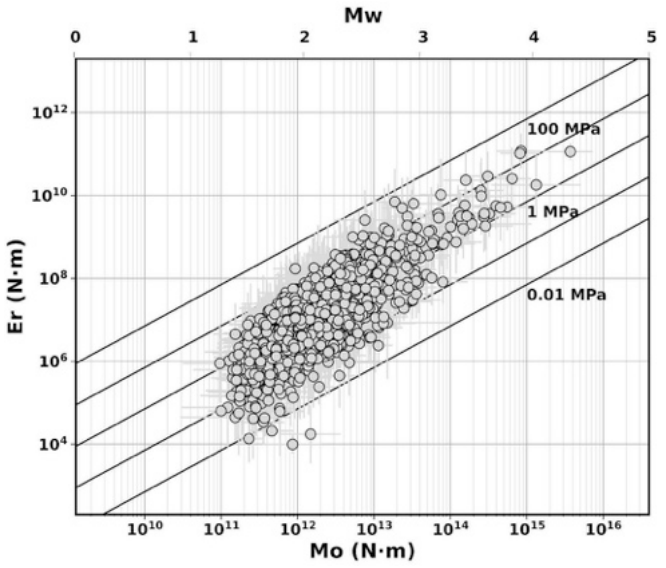

Fig. 11. E_R versus M_0; the solid lines indicate constant apparent stress.

partitioning. According to Kanamori and Rivera (2004), this ratio has a theoretical lower bound and tends to decrease for smaller earthquakes. In our dataset, E_R/M_0 values mostly lie between $\epsilon = 0$ (indicative of self-similar scaling) and $\epsilon = 1$, although significant scatter is observed across the magnitude range (Fig. 12).

Overall, the E_R/M_0 ratios we computed are consistent with those reported for other tectonic settings worldwide (Ide and Beroza, 2001). Although our dataset includes few events with $M_W > 3$, these larger earthquakes generally show ϵ values below 0.5, indicating relatively efficient seismic radiation. In contrast, smaller events exhibit markedly lower E_R/M_0 ratios, suggesting that a larger proportion of their energy is dissipated through non-radiative mechanisms, such as frictional heating, microcracking, or irreversible deformation in the fault zone. Consequently, only a small portion of their total energy budget is radiated as seismic waves.

4.5. Seismic efficiency and dynamic processes

The Savage–Wood seismic efficiency (η_{SW}), defined by Beeler et al. (2003), represents the ratio between apparent stress and static stress drop and is interpreted as a proxy for seismic radiation efficiency. It quantifies the portion of the total stress released during fault rupture that is transformed into radiated seismic energy. In simplified rupture scenarios, $\eta_{SW} = 0.5$ when the dynamic and static stress drops are identical. This value provides an important benchmark for interpreting rupture processes: η_{SW} values <0.5 correspond to overshoot behavior, whereas values >0.5 indicate undershoot conditions (Beeler et al., 2003). Overshoot behavior is characterized by a smaller dynamic stress drop relative to the static stress drop and it is frequently observed in dynamic rupture simulations (e.g., Madariaga, 1976).

Fig. 13 shows the distribution of seismic η_{SW} in our dataset. The median value is 0.28, with a 95 % confidence interval between 0.23 and 0.33, and all values range between 0.10 and 0.69. These values are consistent with a prevailing overshoot behavior. When adopting the source model of Madariaga (1976) instead of Brune (1970), the static stress drop increases by a factor 5.5 (Kaneko and Shearer, 2014) resulting in even lower seismic efficiency. In this case, the median η_{SW} drops to 0.05 (95 % confidence interval: 0.04–0.06), with values ranging between 0.02 and 0.12. According to this model, all events in our dataset fall below the 0.5 threshold, indicating that rupture processes in the SE Alps region are systematically characterized by overshoot dynamics. It is also worth noting that uncertainty in η_{SW} is strongly influenced by uncertainties in stress drop estimates, which are in turn affected by fault geometry and rupture velocity assumptions (Kaneko and Shearer, 2014). This systematic overshoot behavior aligns with the global trends reported by Zúñiga and Rodríguez-Pérez (2025). The strike-slip and normal faulting events often deviate from the predictions of Orowan's model (Orowan, 1960), which relates stress drop to fault slip through a simple elastic dislocation formulation and assumes that rupture ceases once the final stress equals the average dynamic friction, implying a complete stress drop with neither residual nor overshoot stress. Such deviations are linked to elevated apparent stress levels and have significant implications for estimating high-frequency ground motions, further supporting our observations for the Southeastern Alps region.

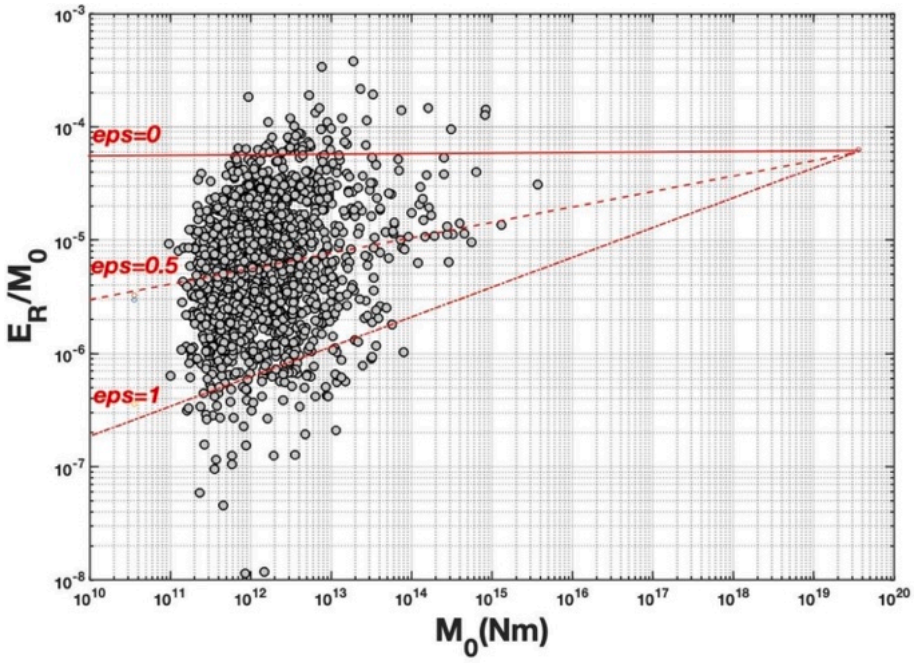

Fig. 12. The E_R/M_0 ratio vs M_0 for the considered dataset; red lines show different types of scaling, computed by assuming a E_R/M_0 ratio of 6.3×10^{-5} for $M_W = 7.0$ (Kanamori and Rivera, 2004). (For interpretation of the references to colour in this figure legend, the reader is referred to the web version of this article.)

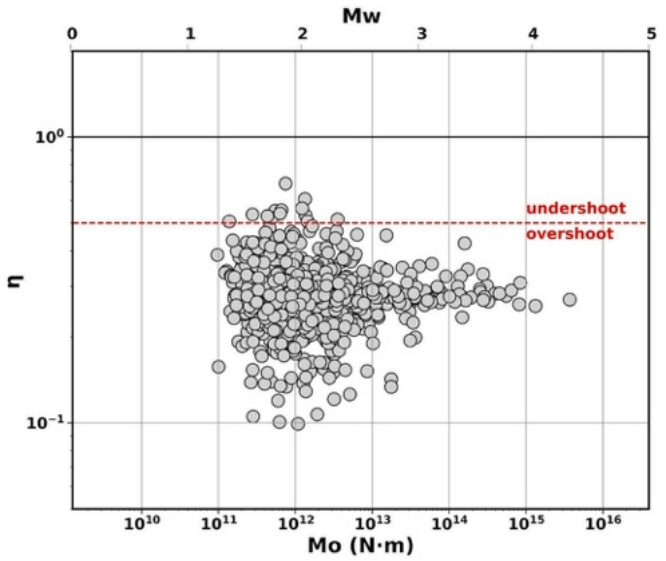

Fig. 13. Seismic moment versus the Savage-Wood seismic efficiency; the red dotted line corresponds to the threshold 0.5, limiting the undershoot from overshoot dynamic weakening mechanisms. (For interpretation of the references to colour in this figure legend, the reader is referred to the web version of this article.)

The dynamic stress drop, $\Delta\sigma_d$, defined as the difference between yield stress and dynamic friction during rupture, can be approximated as $\Delta\sigma_d = \tau_a + \Delta\sigma/2$, if the fracture energy is neglected (Kanamori and Heaton, 2000). Applying this formula to our dataset, we compute $\Delta\sigma_d$ =0.64 Mpa (using Brune) o 2.53 MPa (using Madariaga) . Regardless of the assumed source model, most events fall below the overshoot threshold, further supporting the dominance of this rupture style in the region. The persistently low seismic efficiency suggests that only a limited portion of the total released energy is converted into radiated seismic waves.

The seismic efficiency remains stable for earthquakes with $M_W > 2.5$ while greater variability is observed for smaller events (Fig. 13). This larger scatter at lower magnitudes can be attributed to the influence of local heterogeneities, such as fault roughness, pore pressure, and material contrasts on rupture initiation and propagation. Additionally, estimates of E_R and thus apparent stress, become less reliable for small earthquakes due to lower signal-to-noise ratios, unmodeled source and path effects, and limited bandwidth in the recordings.

5. Conclusions

This study presents one of the most extensive spectral characterizations to date of seismic source parameters in the Southeastern Alps, a tectonically complex region shaped by the convergence of the Eurasian and Adriatic plates. Through single station spectral inversion of more than 1500 well-recorded earthquakes ($1.3 \leq M_W \leq 4.3$) using the SourceSpec software and a dense broadband seismic network, we offer new insights into the physical conditions controlling rupture processes across varied geological settings.

Our results show that earthquake ruptures in the Southeastern Alps slightly deviate from self-similar scaling condition, with static stress drops typically between 0.1 and 10 MPa (median ~ 0.84 MPa), and not evident magnitude dependence. However, radiated energy exhibits a weak magnitude scaling trend, with smaller events appearing less efficient in energy release per unit stress drop, possibly due to greater sensitivity to damage mechanics or near-source heterogeneity at low magnitudes.

One of the most compelling outcomes of our study is the spatial differentiation in source characteristics across the region. In the Western Prealpine Sector and the Eastern Dinaric Margin, earthquakes display elevated stress drops, indicative of more competent crust and efficient energy radiation. These areas may represent stronger, more mature fault zones where seismic ruptures accumulate and release stress more abruptly. In contrast, the Central Alpine Foreland shows systematically lower stress drops and attenuation factors consistent with highly fractured, fluid-rich crust. These observations could suggest a tectonic environment where fluids modulate rupture processes, possibly enhancing aseismic slip or promoting swarm-like behavior.

The apparent stress exceeds 1 MPa for moderate events ($M_W > 2$), pointing to efficient energy radiation at higher magnitudes. However, the overall low seismic efficiency, with median Savage-Wood ratios around 0.28, suggests that rupture in the Southeastern Alps often follows an overshoot rupture regime, where much of the strain energy is dissipated through off-fault processes or frictional heating rather than seismic waves. This inefficiency underscores the importance of fault zone properties such as fluid content, roughness, and structural maturity in controlling rupture dynamics.

We also find that the attenuation quality factor in SE Alps is distributed on a log normal distribution with a median Q_0 of 309. This level of attenuation, coupled with a well-constrained source inversion setup, allows for robust estimates of corner frequencies even in lower-magnitude events, a notable advantage compared to regions with stronger attenuation, where spectral analyses are limited in higher frequencies.

Our results highlight the influence of lithology, fluid content, and fault maturity in modulating source behavior and controlling the partitioning of seismic energy. The stress drop exhibits marked spatial variability that correlates strongly with underlying geological and rheological contrasts reflecting the transitional tectonic regime at the boundary between the Alps and Dinarides.

These findings refine our understanding of seismogenic processes in the region and carry direct implications for seismic hazard assessment. Specifically, areas such as the Western Prealpine Sector and the Eastern Dinaric Margin, which show elevated stress drops, are likely to generate more intense ground shaking for a given magnitude and should be prioritized in future hazard models.

This study demonstrates how high-resolution spectral inversion, combined with tectonic analysis, offers valuable insights into rupture processes and fault zone behavior, while providing reliable, spatially detailed inputs for regional seismic hazard assessment.

CRediT authorship contribution statement

L. Moratto: Conceptualization, Data Curation, Formal analysis, Investigation, Visualization, Writing – original draft, Writing – review & editing. **F. Abi:** Visualization, Writing – review & editing. **A. Saraò:** Conceptualization, Formal analysis, Funding acquisition, Investigation, Visualization, Writing – original draft, Writing – review & editing.

Declaration of competing interest

The authors declare that they have no known competing financial interests or personal relationships that could have appeared to influence the work reported in this paper.

Acknowledgements

Editor, Liang Zhao, and two anonymous reviewers are acknowledged for their constructive comments, which helped in improving this article. SourceSpec (v 1.8) is available at https://sourcespec.readthedocs.io. The map in Fig. 1 has been generated with the Generic Mapping Tools software package (GMT; Wessel et al., 2019); other figures are created with the support of the seismic processing tools of Obspy version 1.4.2 (Beyreuther et al., 2010). This research has been financially supported by the EPOS Research Infrastructure through the contribution of the Italian Ministry of University and Research (MUR). The authors also

gratefully acknowledge the financial support of: Project MEET (Monitoring Earth's Evolution and Tectonics) funded under the National Recovery and Resilience Plan (PNRR); PRIN 2022 project '2022ZHXWC9'—Intercepting the PREparatory Phase of lARge earthquakes from seismic information and gEodetic Displacement (PREPARED); PRIN Project "NASA4SHA" (Fault segmentation and seismotectonics of active thrust systems: the Northern Apennines and Southern Alps laboratories for new Seismic Hazard Assessments in northern Italy).

Data availability

The waveforms utilized in this study are recorded by the following seismic networks: IV (doi:10.13127/sd/x0fxnh7qfy), MN (doi:10.13127/sd/fbbbtdtd6q), NI (doi:https://doi.org/10.7914/SN/NI), OE (doi:https://doi.org/10.7914/SN/OE), OX (doi:https://doi.org/10.7914/SN/OX), 2Y (doi:https://doi.org/10.7914/1p36-6t87), RF (doi:https://doi.org/10.7914/SN/RF), SI (https://www.fdsn.org/networks/detail/SI), SL (doi:https://doi.org/10.7914/SN/SL), and ST (doi:https://doi.org/10.7914/SN/ST). The Bulletin of the Seismometric Network of North Eastern Italy is available at http://www.crs.ogs.it/bollettino_new/ (last accessed December 2024) (in Italian). The processed waveforms utilized in the spectral inversions can be found at doi:https://doi.org/10.5281/zenodo.12794786 (Moratto et al., 2024). The final source parameters can be found at doi:https://doi.org/10.5281/zenodo.16940390 (Moratto et al., 2025a). All these websites were last accessed in December 2025.

References

Abercrombie, R.E., 1995. Earthquake source scaling relationships from −1 to 5 ML using seismograms recorded at 2.5 km depth. J. Geophys. Res. 100, 24015–24036. https://doi.org/10.1029/95jb02397.

Abercrombie, R.E., 2021. Resolution and uncertainties in estimates of earthquake stress drop and energy release. Phil. Trans. R. Soc. A 379, 20200131. https://doi.org/10.1098/rsta.2020.0131.

Abercrombie, R.E., Bannister, S., Ristau, J., Doser, D., 2017. Variability of earthquake stress drop in a subduction setting, the Hikurangi margin, New Zealand. Geophys. J. Int. 208, 306–320. https://doi.org/10.1093/gji/ggw393.

Abercrombie, R.E., Trugman, D.T., Shearer, P.M., Chen, X., Zhang, J., Pennington, C.N., Hardebeck, J.L., Goebel, T.H.W., Ruhlet, C.J., 2021. Does earthquake stress drop increase with depth in the crust? J. Geophys. Res. Solid Earth 126, e2021JB022314. https://doi.org/10.1029/2021JB022314.

Abercrombie, R.E., Baltay, A., Chu, S., Taira, T., Bindi, D., Boyd, O.S., Chen, X., Cochran, E.S., Devin, E., Dreger, D., et al., 2025. Overview of the SCEC/USGS Community stress Drop Validation Study using the 2019 Ridgecrest Earthquake Sequence. Bull. Seismol. Soc. Am. 115, 734–759. https://doi.org/10.1785/0120240158.

Andrews, D.J., 1986. Objective determination of source parameters and similarity of earthquakes of different size. In: Das, S., Boatwright, J., Scholz, C.H. (Eds.), Earthquake Source Mechanics, Vol. 6. American Geophysics Union, Washington D. C., pp. 259–267. https://doi.org/10.1029/GM037p0259. Geophysical Monograph Series.

Aoudia, A., Saraò, A., Bukchin, B., Suhadolc, P., 2000. The 1976 Friuli (NE Italy) thrust faulting earthquake: a reappraisal 23 years later. Geophys. Res. Lett. 27, 573–576. https://doi.org/10.1029/1999GL011071.

Beeler, N.M., Wong, T.F., Hickman, S.H., 2003. On the expected relationships among apparent stress, static stress drop, effective shear fracture energy and efficiency. Bull. Seismol. Soc. Am. 93, 1381–1389. https://doi.org/10.1785/0120020162.

Beyreuther, M., Barsch, R., Krischer, L., Megies, T., Behr, Y., Wassermann, J., 2010. ObsPy: a python toolbox for seismology. Seismol. Res. Lett. 81, 530–533. https://doi.org/10.1785/gssrl.81.3.530.

Bindi, D., Spallarossa, D., Picozzi, M., Morasca, P., 2020. Reliability of source parameters for small events in Central Italy: Insights from spectral decomposition analysis applied to both synthetic and real data. Bull. Seismol. Soc. Am. 202, 3139–3157. https://doi.org/10.1785/0120200126.

Bindi, D., Spallarossa, D., Picozzi, M., Tarchini, G., 2024. Scaling and depth variability of source parameters in Central and Southern Italy using regional attenuation models. Bull. Seismol. Soc. Am. 115, 983–999. https://doi.org/10.1785/0120240144.

Boatwright, J., Choy, G.L., Seekins, L.C., 2002. Regional estimates of radiated seismic energy. Bull. Seismol. Soc. Am. 92, 1241–1255. https://doi.org/10.1785/0120000932.

Bragato, P.L., Sugan, M., Augliera, P., Massa, M., Vuan, A., Saraò, A., 2011. Moho reflection effects in the Po plain (northern Italy) observed from instrumental and intensity data. Bull. Seismol. Soc. Am. 101, 2142–2152. https://doi.org/10.1785/0120100257.

Bragato, P.L., Comelli, P., Saraò, A., Zuliani, D., Moratto, L., Poggi, V., Rossi, G., Scaini, C., Sugan, M., Barnaba, C., Bernardi, P., Bertoni, M., Bressan, G., Compagno, A., Del Negro, E., Di Bartolomeo, P., Fabris, P., Garbin, M., Grossi, M., Magrin, A., Magrin, E., Pesaresi, D., Petrovic, B., Plasencia Linares, M.P., Romanelli, M., Snidarcig, A., Tunini, L., Urban, S., Venturini, E., Parolai, S., 2021. The OGS- North-Eastern Italy seismic and de- formation network: current status and outlook. Seismol. Res. Lett. 92, 1704–1716. https://doi.org/10.1785/0220200372.

Bressan, G., Bragato, P.L., Venturini, C., 2003. Stress and strain tensors based on focal mechanisms in the seismotectonic framework of the Friuli–Venezia Giulia region (north-eastern Italy). Bull. Seismol. Soc. Am. 93, 1280–1297. https://doi.org/10.1785/0120020058.

Bressan, G., Kravanja, S., Franceschina, G., 2007. Source parameters and stress release of seismic sequences occurred in the Friuli-Venezia Giulia region (Northeastern Italy) and in Western Slovenia. Phys. Earth Planet. Inter. 160, 192–214. https://doi.org/10.1016/j.pepi.2006.10.005.

Bressan, G., Barnaba, C., Bragato, P., Ponton, M., Restivo, A., 2018. Revised seismotectonic model of NE Italy and W Slovenia based on focal mechanism inversion. J. Seismol. 22, 1563–1578. https://doi.org/10.1007/s10950-018-9785-2.

Bressan, G., Barnaba, C., Bragato, P.L., Peresan, A., Rossi, G., Urban, S., 2019. Distretti sismici del Friuli Venezia Giulia (NE Italy). Boll. Geofis. Teor. Appl. 60 (3), s1–s74. https://doi.org/10.4430/bgta0300.

Brondi, P., Snidarcig, A., Bernardi, P., Bragato, P.L., Di Bartolomeo, P., 2024. Bollettino della Rete Sismometrica dell'Italia Nord Orientale (RSINO), Anno 2022 [Data set]. In: Istituto Nazionale di Oceanografia e di Geofisica Sperimentale – OGS. https://doi.org/10.13120/w1vp-b578 (in Italian).

Brondi, P., Snidarcig, A., Di Bartolomeo, P., Magrin, A., Barnaba, C., Poggi, V., Pettenati, F., Romanelli, M., Rebez, A., Moratto, L., Sandron, D., Plasencia, M., Pesaresi, D., Compagno, A., Del Negro, E., Comelli, P., Magrin, E., Zuliani, D., Bertoni, M., Fabris, P., Bernardi, P., 2025. Bollettino della Rete Sismometrica dell'Italia Nord Orientale (RSINO), Anno 2023 [Data set]. In: Istituto Nazionale di Oceanografia e di Geofisica Sperimentale - OGS. https://doi.org/10.13120/m4pk-nd81(in Italian).

Brune, J., 1970. Tectonic stress and the spectra of seismic shear waves from earthquakes. J. Geophys. Res. 75, 4997–5009. https://doi.org/10.1029/JB075i026p04997.

Cataldi, L., Poggi, V., Costa, G., Parolai, S., Edwards, B., 2023. Parametric spectral inversion of seismic source, path and site parameters: application to Northeast Italy. Geophys. J. Int. 232, 1926–1943. https://doi.org/10.1093/gji/ggac431.

Deichmann, N., 2018. The relation between M_E, M_L and M_W in theory and numerical simulations for small to moderate earthquakes. J. Seismol. 22, 1645. https://doi.org/10.1007/s10950-018-9786-1.

Eberhart-Phillips, D., Chadwick, M., 2002. Three-dimensional attenuation model of the shallow Hikurangi subduction zone in the Raukumara Peninsula, New Zealand. J. Geophys. Res. 107. https://doi.org/10.1029/2000JB000046.

Folesky, J., 2024. Different earthquake nucleation conditions revealed by stress drop and b-value mapping in the northern Chilean subduction zone. Sci. Rep. 14, 12182. https://doi.org/10.1038/s41598-024-63015-w.

Franceschina, G., Kravanja, S., Bressan, G., 2006. Source parameters and scaling relationships for earthquakes in NE Italy. Phys. Earth Planet. Inter. 154, 148–167. https://doi.org/10.1016/j.pepi.2005.09.004.

Franceschina, G., Gentili, S., Bressan, G., 2013. Source parameters scaling of the 2004 Kobarid (Western Slovenia) seismic sequence. Phys. Earth Planet. Inter. 222, 58–75. https://doi.org/10.1016/j.pepi.2013.07.004.

Goebel, T.H.W., Hauksson, E., Shearer, P.M., Ampuero, J.P., 2015. Stress-drop heterogeneity within tectonically complex regions: a case study of San Gorgonio Pass, southern California. Geophys. J. Int. 202, 514–528. https://doi.org/10.1093/gji/ggv160.

Ide, S., Beroza, G.C., 2001. Does apparent stress vary with earthquake size? Geophys. Res. Lett. 28, 3349–3352. https://doi.org/10.1029/2001GL013106.

Jolivet, R., Frank, W.B., 2020. The transient and intermittent nature of slow slip. AGU Adv. 1, e2019AV000126. https://doi.org/10.1029/2019AV000126.

Jozi Najafabadi, A., Haberland, C., Handy, M.R., Le Breton, E., Weber, M., 2023. Seismic wave attenuation (1/Qp) in the crust underneath the Eastern and eastern Southern Alps (Europe): imaging effects of faults, fractures, and fluids. Earth Planets Space 75, 187. https://doi.org/10.1186/s40623-023-01942-0.

Kanamori, H., Heaton, T.H., 2000. Microscopic and macroscopic physics of earthquakes. In: GeoComplexity and the Physics of Earthquakes. In: Geophysical Monograph, 120. AGU, Washington, D. C, pp. 147–163 doi:10.1029/GM120p0147.

Kanamori, H., Rivera, L., 2004. Static and dynamic scaling relations for earthquakes and their implications for rupture speed and stress drop. Bull. Seismol. Soc. Am. 94, 314–319. https://doi.org/10.1785/012003015.

Kaneko, K., Shearer, P.M., 2014. Seismic source spectra and estimated stress drop derived from cohesive-zone models of circular subshear rupture. Geophys. J. Int. 197, 1002–1015. https://doi.org/10.1093/gji/ggu030.

Klin, P., Laurenzano, G., Barnaba, C., Priolo, E., Parolai, S., 2021. Site Amplification at Permanent Stations in Northeastern Italy. Bull. Seismol. Soc. Am. 111, 1885–1904. https://doi.org/10.1785/0120200361.

Lancieri, M., Madariaga, R., Bonilla, F., 2012. Spectral scaling of the aftershocks of the Tocopilla 2007 earthquake in northern Chile. Geophys. J. Int. 189, 469–480. https://doi.org/10.1111/j.1365-246X.2011.05327.x.

Lanzoni, A., Moratto, L., Priolo, E., Romano, M.A., 2020. Fast Mw estimation of microearthquakes recorded around the underground gas storage in the Montello-Collalto area (Southeastern Alps, Italy). J. Seismol. 24, 1029–1043. https://doi.org/10.1007/s10950-019-09889-0.

Lengliné, O., Schmittbuhl, J., Drif, K., Lambotte, S., Grunberg, M., Kinscher, J., Sira, C., Schlupp, A., Schaming, M., Jund, H., Masson, F., 2023. The largest induced earthquakes during the GEOVEN deep geothermal project, Strasbourg, 2018–2022:

from source parameters to intensity maps. Geophys. J. Int. 234, 2445–2457. https://doi.org/10.1093/gji/ggad255.
Madariaga, R., 1976. Dynamics of an expanding circular fault. Bull. Seismol. Soc. Am. 66, 639–666. https://doi.org/10.1785/BSSA0660030639.
Madariaga, R., 2011. Earthquake scaling laws. In: Extreme Environmental Events. Springer, New York, New York, NY, pp. 364–383 doi:10.1007/978-1-4419-7695-6_22.
Malagnini, L., Akinci, A., Herrmann, R.B., Pino, N.A., Scognamiglio, L., 2002. Characteristics of the ground motion in Northeastern Italy. Bull. Seismol. Soc. Am. 92, 2186–2204. https://doi.org/10.1785/0120010219.
Moratto, L., Sandron, D., 2015. Optimizing the automatic location of the real-time Antelope® system in North-Eastern Italy. Boll. Geofis. Teor. Appl. 56, 407–424. https://doi.org/10.4430/bgta0154.
Moratto, L., Saraò, A., Priolo, E., 2017. Moment magnitude (Mw) estimation of weak seismicity in Northeastern Italy. Seismol. Res. Lett. 88, 1455–1464. https://doi.org/10.1785/0220170063.
Moratto, L., Romano, M.A., Laurenzano, G., Colombelli, S., Priolo, E., Zollo, A., Saraò, A., Picozzi, M., 2019. Source parameter analysis of microearthquakes recorded around the underground gas storage in the Montello-Collalto Area (Southeastern Alps, Italy). Tectonophysics 762, 159–168. https://doi.org/10.1016/j.tecto.2019.04.030.
Moratto, L., Tarchini, G., Saraò, A., 2024. Catalog of NE Italy earthquakes Mw with related velocimetric time series [Data set]. In: Zenodo. https://doi.org/10.5281/zenodo.12794785.
Moratto, L., Saraò, A., 2025a. Catalog of source parameters estimated for earthquakes occurred in Southeastern Alps (1.0.0) [Data set]. Zenodo, doi: https://doi.org/10.5281/zenodo.16940390.
Moratto, L., Panebianco, S., Satriano, C., Stabile, T.A., Priolo, E., 2025b. Using ambient noise k_0 estimation to improve microearthquakes source parameters assessment in the High Agri Valley. Geophys. J. Int. 242 (2), ggaf191. https://doi.org/10.1093/gji/ggaf191 ggaf191.
Moyer, P.A., Boettcher, M.S., McGuire, J.J., Collins, J.A., 2018. Spatial and temporal variations in earthquake stress drop on Gofar Transform Fault, East Pacific rise: Implications for fault strength. J. Geophys. Res. Solid Earth 123, 7722–7740. https://doi.org/10.1029/2018JB015942.
Orowan, E., 1960. Mechanism of seismic faulting in rock deformation. Geol. Soc. Am. Memoir 79, 323–345. https://doi.org/10.1130/MEM79-p323.
Oth, A., 2013. On the characteristics of earthquake stress release variations in Japan. Earth Planet. Sci. Lett. 377–378, 132–141. https://doi.org/10.1016/j.epsl.2013.06.037.
Panebianco, S., Serlenga, V., Satriano, C., Cavalcante, F., Stabile, T.A., 2023. Semi-automated template matching and machine-learning based analysis of the August 2020 Castelsaraceno microearthquake sequence (southern Italy). Geomat. Nat. Haz. Risk 14, 2207715. https://doi.org/10.1080/19475705.2023.2207715.
Pérez-Campos, X., Beroza, G.C., 2001. An apparent mechanism dependence of radiated seismic energy. J. Geophys. Res. 106 (B6), 11127–11136. https://doi.org/10.1029/2000JB900455.
Priolo, E., Laurenzano, G., Barnaba, C., Bernardi, P., Moratto, L., Spinelli, A., 2015. OASIS - the OGS archive system of instrumental seismology. Seismol. Res. Lett. 86, 978–984. https://doi.org/10.1785/0220140175.
Rajh, G., Stipcevic, J., Zivcic, M., Herak, M., Gosar, A., the AlpArray Working Group, 2024. Investigation of the Upper Crustal Structure in the NW Dinarides using local Earthquake Tomography. ESS Open Archive. https://doi.org/10.22541/essoar.171838389.91461123/v1.
Rietbrock, A., 2001. P wave attenuation structure in the fault area of the 1995 Kobe earthquake. J. Geophys. Res. 106, 4141–4154. https://doi.org/10.1029/2000jb900234.
Saadalla, H., Qaysi, S., Ezzelarab, M., Abdelnabi, A., Sehli, T., 2025. Estimating dynamic source parameters from S-Wave spectra for earthquakes in the Dahshour Region, Northwestern Egypt. J. Seismol. 29, 643–659. https://doi.org/10.1007/s10950-025-10297-w.
Saraò, A., Sugan, M., Bressan, G., Renner, G., Restivo, A., 2021. A focal mechanism catalogue of earthquakes that occurred in the southeastern Alps and surrounding areas from 1928–2019. Earth Syst. Sci. Data 13, 2245–2258. https://doi.org/10.5194/essd-13-2245-2021.
Satriano, C., 2024. SourceSpec – Earthquake Source Parameters from P- or S-Wave Displacement Spectra (1.8). https://doi.org/10.5281/ZENODO.3688587.
Scherbaum, F., 1990. Combined inversion for the three-dimensional Q structure and source parameters using microearthquake spectra. J. Geophys. Res. 95, 12423–12438. https://doi.org/10.1029/JB095iB08p12423.
Scherbaum, F., 1994. Modelling the Roermond earthquake of 1992 April 13 by stochastic simulation of its high-frequency strong ground motion. Geophys. J. Int. 119 (1), 31–43. https://doi.org/10.1111/j.1365-246X.1994.tb00911.x.
Shearer, P.M., Prieto, G.A., Hauksson, E., 2006. Comprehensive analysis of earthquake source spectra in southern California. J. Geophys. Res. Solid Earth 111, B06303. https://doi.org/10.1029/2005JB003979.
Slejko, D., Carulli, G.B., Nicolich, R., Rebez, A., Zanferrari, A., Cavallin, A., Doglioni, C., Carraro, F., Castaldini, D., Illiceto, V., et al., 1989. Seismotectonics of the Eastern Southern-Alps: a review. Boll. Geofis. Teor. Appl. 31, 109–136.
Slejko, D., Carulli, G.B., Riuscetti, M., Cucchi, F., Grimaz, S., Rebez, A., Accaino, F., Affatato, A., Biolchi, S., Nieto, D., Puntel, E., Sanò, T., Santulin, M., Tinivella, U., Zini, L., 2011. Soil characterization and seismic hazard maps for the Friuli-Venezia Giulia Region (NE Italy). Boll. Geofis. Teor. Appl. 52, 59–104.
Snidarcig, A., Bernardi, P., Bragato, P.L., Di Bartolomeo, P., Garbin, M., Urban, S., 2017. Bollettino della Rete Sismometrica dell'Italia Nord Orientale (RSINO), Anno 2016 [Data set]. In: Istituto Nazionale di Oceanografia e di Geofisica Sperimentale – OGS, Trieste, Italy. https://doi.org/10.6092/a608d853-755e-4177-aada-992857ccb44e (in Italian).
Snidarcig, A., Bernardi, P., Bragato, P.L., Di Bartolomeo, P., Garbin, M., Urban, S., 2018. Bollettino della Rete Sismometrica dell'Italia Nord Orientale (RSINO), Anno 2017 [Data set]. In: Istituto Nazionale di Oceanografia e di Geofisica Sperimentale – OGS, Trieste, Italy. https://doi.org/10.6092/3ff3c323-d7a4-4183-bea0-1a53814ac8b9 (in Italian).
Snidarcig, A., Bernardi, P., Bragato, P.L., Di Bartolomeo, P., Garbin, M., Urban, S., 2019. Bollettino della Rete Sismometrica dell'Italia Nord Orientale (RSINO), Anno 2018 [Data set]. In: Istituto Nazionale di Oceanografia e di Geofisica Sperimentale – OGS, Trieste, Italy. https://doi.org/10.6092/c53f37ce-bcf3-453c-a2cf-1894d48cfbbb.
Snidarcig, A., Bernardi, P., Bragato, P.L., Di Bartolomeo, P., Garbin, M., Urban, S., 2020. Bollettino della Rete Sismometrica dell'Italia Nord Orientale (RSINO), Anno 2019 [Data set]. In: Istituto Nazionale di Oceanografia e di Geofisica Sperimentale – OGS, Trieste, Italy. https://doi.org/10.6092/58ff169a-2f02-46ae-908a-bdfcacea069c (in Italian).
Snidarcig, A., Bernardi, P., Bragato, P.L., Di Bartolomeo, P., Garbin, M., Urban, S., 2021. Bollettino della Rete Sismometrica dell'Italia Nord Orientale (RSINO), Anno 2020 [Data set]. In: Istituto Nazionale di Oceanografia e di Geofisica Sperimentale – OGS, Trieste, Italy. https://doi.org/10.13120/108b8d94-361a-45f3-8195-fc4e8f73d264 (in Italian).
Snidarcig, A., Bernardi, P., Bragato, P.L., Di Bartolomeo, P., Garbin, M., Urban, S., Urban, 2022. Bollettino della Rete Sismometrica dell'Italia Nord Orientale (RSINO), Anno 2021 [Data set]. In: Istituto Nazionale di Oceanografia e di Geofisica Sperimentale – OGS, Trieste, Italy. https://doi.org/10.13120/8b252b09-314f-456f-812a-b05268ecd001 (in Italian).
Sugan, M., Peruzza, L., 2011. Distretti sismici del Veneto. Boll. Geofis. Teor. Appl. 52 (1), s3–s90. https://doi.org/10.4430/bgta0057.
Sugan, M., Saraò, A., Magrin, A., Snidarcig, A., Bressan, G., Renner, G., Romano, M.A., Guidarelli, M., Santulin, M., Di Bartolomeo, P., Restivo, A., 2024. Focal mechanisms of the Southeastern Alps and surroundings (2.0) [Data set]. In: Zenodo. https://doi.org/10.5281/zenodo.10853582.
Tarchini, G., Moratto, L., Saraò, A., 2025. A Comprehensive Moment Magnitude catalog for the Northeastern Italy Region. Seismol. Res. Lett. 96, 2714–12723. https://doi.org/10.1785/0220240303.
Wang, Z., Liu, R., Liu, W., 2023. Source characteristics of the aftershocks of the Wenchuan and Lushan earthquake sequences in the Longmen-Shan fault zone. Front. Earth Sci. 10, 1061754. https://doi.org/10.3389/feart.2022.1061754.
Wessel, P., Luis, J.F., Uieda, L., Scharroo, R., Wobbe, F., Smith, W.H.F., Tian, D., 2019. The generic mapping tools version 6. Geochem. Geophys. Geosyst. 20 (11), 5556–5564. https://doi.org/10.1029/2019GC008515.
Wyss, M., 1979. Observation and Interpretation of Tectonic Strain Release Mechanisms. PhD thesis. Calif. Inst. of Technol, Pasadena.
Yen, M.H., Bindi, D., Oth, A., Edwards, B., Zaccarelli, R., Cotton, F., 2024. Source parameters and scaling relationships of stress drop for shallow crustal seismic events in Western Europe. J. Seismol. 28, 63–79. https://doi.org/10.1007/s10950-023-10188-y.
Zollo, A., Orefice, A., Convertito, V., 2014. Source parameter scaling and radiation efficiency of microearthquakes along the Irpinia fault zone in southern Apennines, Italy. J. Geophys. Res. Solid Earth 119. https://doi.org/10.1002/2013JB010116.
Zúñiga, F.R., Rodríguez-Pérez, Q., 2025. Stress differences and their role in identifying earthquake source process properties at different tectonic environments. J. Seismol. 29, 337–352. https://doi.org/10.1007/s10950-025-10286-z.